

ARTICLE OPEN



Creatine transporter (SLC6A8) knockout mice exhibit reduced muscle performance, disrupted mitochondrial Ca^{2+} homeostasis, and severe muscle atrophy

Irene Pertici^{1,9}, Donato D'Angelo^{2,9}, Denis Vecellio Reane³, Massimo Reconditi¹, Ilaria Morotti¹, Elena Putignano⁴, Debora Napoli⁴, Giorgia Rastelli⁵, Gaia Gherardi², Agnese De Mario², Rosario Rizzuto^{2,6}, Simona Boncompagni⁵, Laura Baroncelli^{4,7}, Marco Linari¹, Marco Caremani¹ and Anna Raffaello^{2,8}

© The Author(s) 2025

Creatine (Cr) is essential for cellular energy homeostasis, particularly in muscle and brain tissues. Creatine Transporter Deficiency (CTD), an X-linked disorder caused by mutations in the SLC6A8 gene, disrupts Cr transport, leading to intellectual disability, speech delay, autism, epilepsy, and various non-neurological symptoms. In addition to neurological alterations, Creatine Transporter knockout (CrT^{-/-}) mice exhibit severe muscle atrophy and functional impairments. This study provides the first characterization of the skeletal muscle phenotype in CrT^{-/-} mice, revealing profound ultrastructural abnormalities accompanied by reduced fiber cross-sectional area and muscle performance. Notably, mitochondria are involved, as evidenced by disrupted cristae, increased mitochondrial size, impaired Ca^{2+} uptake, reduced membrane potential and ATP production. Mechanistically, the expression of atrophy-specific E3 ubiquitin ligases and suppression of the IGF1-Akt/PKB pathway, regulated by mitochondrial Ca^{2+} levels, further support the atrophic phenotype. These findings highlight the profound impact of Cr deficiency on skeletal muscle, emphasizing the need for targeted therapeutic strategies to address both the neurological and peripheral manifestations of CTD. Understanding the underlying mechanisms, particularly mitochondrial dysfunction, could lead to novel interventions for this disorder.

Cell Death and Disease (2025)16:99; <https://doi.org/10.1038/s41419-025-07381-x>

INTRODUCTION

Creatine (Cr) plays a crucial role in regulating cellular energy homeostasis, particularly in high-demanding tissues such as the muscle and the brain [1]. Creatine Kinase (CK) converts Cr into phospho-creatine (PCr), a metabolically inert phosphagen used for temporal and spatial buffering of ATP levels. The PCr/CK system is vital for high-intensity physical exercise in striated muscle and heart contraction when ATP hydrolysis exceeds production by other metabolic pathways [2, 3].

Approximately one-half of the daily Cr needs in humans comes from the diet, with the remaining one-half synthesized endogenously through a two-step enzymatic pathway involving L-arginine:glycine amidinotransferase (AGAT) and S-adenosyl-L-methionine:N-guanidinoacetate methyltransferase (GAMT) mostly in the liver, pancreas, and kidneys [3, 4]. After synthesis or nutritional supply, Cr is released into the bloodstream to nourish all body cells. However, Cr cannot cross the lipid membrane and requires a specific Na^+/Cl^- -dependent transporter (Cr transporter, CrT). In humans, CrT is predominantly

expressed in the muscle, kidney, heart, and other tissues, including the brain [5–7].

Creatine Transporter Deficiency (CTD, OMIM #300352) is a monogenic X-linked disorder [8], associated with multiple mutations in the solute carrier family 6-member 8 (Slc6a8) gene that encodes the protein responsible for cellular Cr transport [8, 9]. Recent studies suggest that the prevalence of this disorder might range between 1% and 3% in males with intellectual disability [8, 10]. However, the lack of prenatal and perinatal screening makes CTD a still underdiagnosed disorder. Clinical hallmarks include intellectual disability, severe speech delay, autistic features, epilepsy, and movement disorders [9]. Patients also experience non-neurological symptoms, including gastrointestinal dysfunction, bladder dysfunction, cardiomyopathy, and ophthalmologic abnormalities [11, 12]. Skeletal muscle mass reduction and mild muscle weakness have been described [12, 13], primarily as late onset deficits [14–16]. While Cr concentration in skeletal muscle appears to be within the normal range, this has only been analyzed for a few specific mutations [17, 18].

¹Physiolab (Department of Biology and Department of Experimental and Clinical Medicine), University of Florence, Florence, Italy. ²Department of Biomedical Sciences, University of Padova, Padova, Italy. ³Institute for Diabetes and Obesity, Helmholtz Diabetes Center, Helmholtz Zentrum Munich, Munich, Germany. ⁴Institute of Neuroscience, National Research Council (CNR), Pisa, Italy. ⁵Center for Advanced Studies and Technology, Department of Neuroscience, Imaging, and Clinical Sciences, University G. D'Annunzio of Chieti-Pescara, Chieti, Italy. ⁶National Center of Gene Therapy and RNA-based Drugs, Padova, Italy. ⁷Department of Developmental Neuroscience, IRCCS Stella Maris Foundation, Pisa, Italy. ⁸Myology Center (CIR-Myo), University of Padua, Padua, Italy. ⁹These authors contributed equally: Irene Pertici, Donato D'Angelo. ✉email: marco.caremani@unifi.it; anna.raffaello@unipd.it

Edited by Professor Paolo Pinton

Received: 14 August 2024 Revised: 17 December 2024 Accepted: 22 January 2025

Published online: 14 February 2025

The absence of a functional CrT renders Cr supplementation ineffective for CTD [8]. Consequently, effective treatments for CTD remain elusive, posing ongoing challenges for patients and their families.

To understand the causative mechanisms and the main molecular pathways altered in CTD, animal models lacking the *Slc6a8* gene or engineered to express an allele with the point mutation found in patients have been generated [19–22]. These rodent lines have significantly contributed to dissecting the pathological determinants of this disorder [8]. They revealed that the loss-of-function of *Slc6a8* does not result in overt alterations in brain structure and neuronal density but rather in a subtle reorganization of cerebral circuits and cellular metabolic processes [19, 22–24]. However, the cellular and molecular players involved in the development and progression of the CTD phenotype, not only in the brain but also in skeletal muscle, remain largely unexplored [8].

Interestingly, unlike CTD patients, skeletal muscles of CrT knockout ($\text{CrT}^{-/y}$) animals exhibit low Cr levels and a severely compromised phenotype, characterized by impaired motor function, muscle atrophy, increased glucose metabolism due to AMPK activation [21, 25], and susceptibility to fatigue [26]. Motor alterations are absent in mice harboring a brain-specific *Slc6a8* deletion, suggesting a peripheral contribution to the onset of CTD pathology [27, 28]. Nevertheless, a complete description of the skeletal muscle phenotype and the underlying mechanisms remain elusive. The study of this aspect is particularly important given that the PCr-CK system requires high levels of total Cr (20–40 mM) in skeletal muscle [29] that can be achieved only with functional cellular Cr uptake [29].

Interestingly, CTD clinical phenotype closely resembles that observed in a wide range of mitochondrial disorders (e.g., developmental, or cognitive disabilities, seizures, fatigue and cardiomyopathy). CTD patients initially suspected of having a mitochondrial disorder were later found to have a creatine transporter defect. Notably, there is a strong link between Cr and mitochondrial function, and changes in PCr/Cr ratio finely regulate mitochondrial respiration [1, 30–32]. It is thus not surprising that the metabolic phenotype of Cr deficiency results in disturbed metabolic activity, as well as structural abnormalities of mitochondrial organelles [24, 28, 33, 34]. Nevertheless, mitochondrial abnormalities and their causative role in the pathogenesis of this disease have scarcely been assessed at functional and molecular levels. This is a crucial aspect, as preclinical evidence suggests that mitochondria might be promising targets for therapeutic intervention in various brain and motor dysfunctions.

In this study, we describe the profound impact of Cr deficiency on the skeletal muscle of $\text{CrT}^{-/y}$ animals. Specifically, we found that muscles exhibit an atrophic phenotype accompanied by fibers ultrastructural alterations, diminished performance, and increased expression of key E3 ubiquitin ligases associated with the progression of atrophy. Additionally, mitochondria display significant morphological abnormalities, reduced membrane potential, and impaired mitochondrial Ca^{2+} uptake, accompanied by changes in the expression of proteins involved in mitochondrial Ca^{2+} homeostasis.

RESULTS

$\text{CrT}^{-/y}$ muscles exhibit pronounced fiber atrophy and ultrastructural alterations

The mouse model carrying the ubiquitous deletion of 5–7 exons in the *Slc6a8* gene ($\text{CrT}^{-/y}$ knockout, $\text{CrT}^{-/y}$) [20] exhibits low Cr levels in the brain, skeletal and cardiac muscles, and kidneys [20, 23]. Given that no comprehensive characterization of skeletal muscle structure has been performed in this model thus far and considering the crucial role of Cr in muscle metabolism, we began by assessing the presence of qualitative and quantitative

ultrastructure alterations. Using Transmission Electron Microscopy (TEM), we analyzed the Extensor Digitorum Longus (EDL) muscle in WT and $\text{CrT}^{-/y}$ mice at Post Natal Day (PND) 40. In WT mice, the average cross-sectional area (CSA) of the fibers is $970 \pm 16 \mu\text{m}^2$ (mean \pm SEM) (Fig. 1A, gray columns and Fig. 1B), while in $\text{CrT}^{-/y}$ mice the CSA of the fibers is significantly reduced to $280 \pm 3 \mu\text{m}^2$ (Fig. 1A blue columns and Fig. 1B). The number of fibers per $1000 \mu\text{m}^2$ is 0.9 ± 0.1 in WT mice, resulting in a fractional area of the muscle occupied by the fibers of $[(970 \mu\text{m}^2/\text{fiber})/(1000 \mu\text{m}^2/0.9 \text{ fibers})] = 0.87 \pm 0.10$ (Fig. 1B). In $\text{CrT}^{-/y}$ mice, with 2.2 ± 0.5 fibers per $1000 \mu\text{m}^2$ (Fig. 1B), the fractional area is the muscle occupied by the fibers is 0.62 ± 0.16 (Fig. 1B), approximately 30% lower than in WT mice. $\text{CrT}^{-/y}$ muscles exhibit an increased fraction of intermyofibrillar space relative to fiber volume (0.292 ± 0.009) compared to WT muscles (0.155 ± 0.007), resulting in a decreased fractional fiber volume (0.708 ± 0.016 in $\text{CrT}^{-/y}$ mice and 0.845 ± 0.014 in WT mice, Fig. 1C, D). The CSA occupied by the myofibrils within the muscle can be determined multiplying the CSA of the EDL muscle, estimated from the wet weight of the muscle (see Methods), by a factor $a = 0.87 \times 0.845 = 0.74 \pm 0.08$ (or 74%) for the WT mice and $0.62 \times 0.708 = 0.44 \pm 0.10$ (or 44%) for the $\text{CrT}^{-/y}$ mice.

Muscle performance impairments and myosin heavy chain isoform shifts in $\text{CrT}^{-/y}$ mice

We then investigated whether the observed morphological alterations affected muscle performance. Consistent with the structural changes, grip strength in $\text{CrT}^{-/y}$ mice showed a significant reduction, with strength diminished to 45% and 10% of that in WT mice at PND 40 and 90, respectively (Fig. 2A). Additionally, the isometric force (T_0) of EDL muscles from PND40 $\text{CrT}^{-/y}$ mice was substantially lower, measuring 71 ± 3 mN, which is just $18 \pm 1\%$ of the WT mice's force (395 ± 14 mN, Fig. 2D).

To further assess muscle performance, we analyzed the force-velocity (T - V) and the power-force (P - T) relations. The shortening velocity (V), measured following a drop in force from T_0 to a pre-set value T lower than T_0 (Supplementary Fig. 1A), was significantly reduced for $T < 0.4T_0$ in $\text{CrT}^{-/y}$ mice compared with WT mice (Supplementary Fig. 1B). This reduction was accompanied by a decrease in the curvature of the T - V relation (increase in a/T_0^* , see Methods and Fig. 2), approximately two-fold, and a reduction in the unloaded shortening velocity (V_{max}) from $4.4 \pm 0.1 L_0/s$ in WT mice to $3.0 \pm 0.1 L_0/s$ in $\text{CrT}^{-/y}$ mice, with L_0 representing the initial muscle length (Fig. 2B, D, and Supplementary Fig. 1B). Power output ($P = T \times V$) at any T was lower in $\text{CrT}^{-/y}$ mice compared to WT mice (Fig. 2C). The maximum power output (P_{max}), achieved at about one-third of the maximum force, was reduced to approximately 14% of WT levels (from 1.83 ± 0.09 mW to 0.25 ± 0.03 mW, Fig. 2C, D).

The reduced muscle performance could be linked to a shift of the myosin heavy chain (MHC) isoforms expressed in the EDL muscle. The MHC-2X:MHC-2B ratio is 2:3 in the WT mice and 1:1 in the $\text{CrT}^{-/y}$ mice with a shift in the expression of the faster MHC-2B isoform to the slower MHC-2X isoform (Fig. 2E–G). Considering that fibers expressing pure MHC-2B and MHC-2X isoforms have similar isometric force while the unloaded shortening velocity of the fibers expressing the MHC-2X isoform is about $\frac{1}{2}$ of those expressing the MHC-2B isoform [35], the lower V_{max} found in the EDL muscle of mutated mice could be explained by the increased expression of the slower MHC-2X isoform with respect to the faster MHC-2B isoform. However, the shift in the MHC isoforms alone would not fully account for the reduction in P_{max} (Supplementary Fig. 1C). Therefore, other factors, such as fiber atrophy, structural alterations of sarcomeres, or altered Ca^{2+} handling, must contribute to the reduced muscle performance.

Focusing on Ca^{2+} dynamics, we measured cytosolic Ca^{2+} concentration $[\text{Ca}^{2+}]_{\text{cyt}}$ on isolated Flexor Digitorum Brevis (FDB) fibers upon caffeine stimulation using Fura-2/AM. While resting

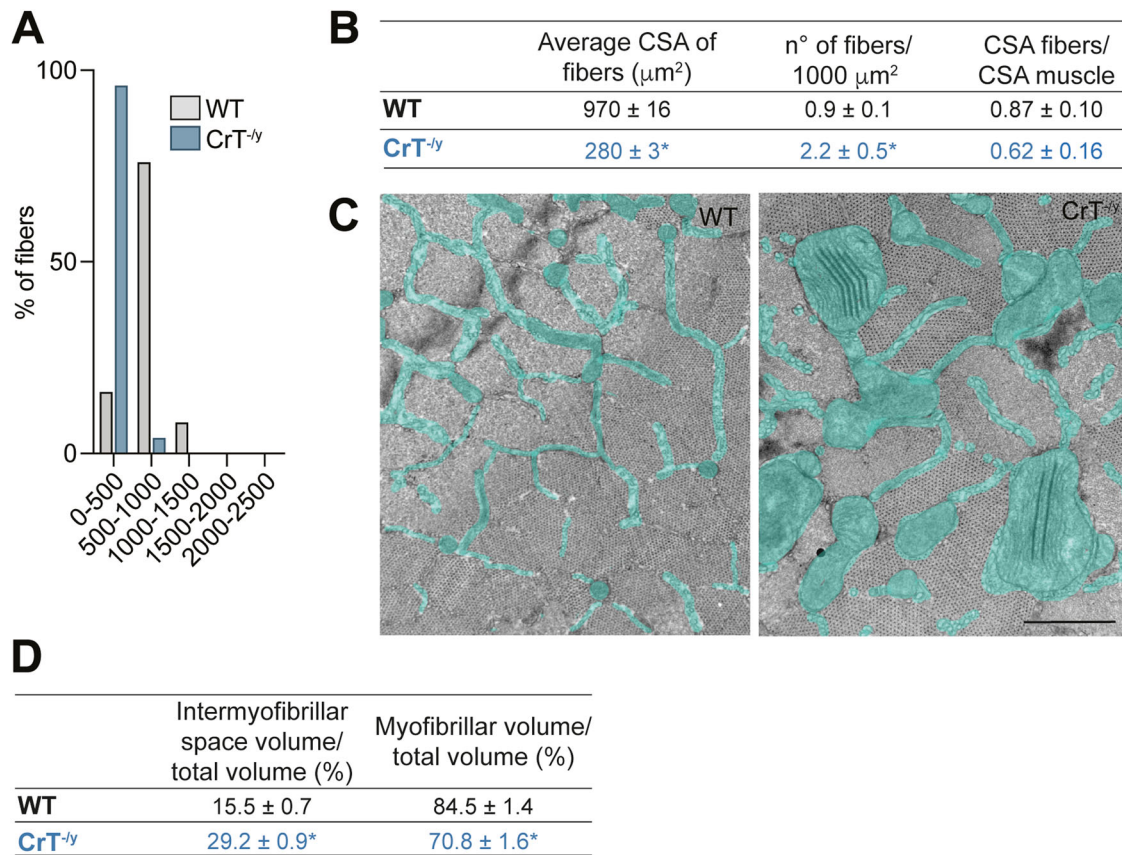


Fig. 1 Quantification of the amount of contractile material in EDL muscle from WT and CrT^{-/-} mice. **A** Distribution of the cross-sectional area of the fibers in the EDL muscle of WT and CrT^{-/-} mice. Samples size: 3 EDLs for each group. **B** Cross-sectional area occupied by the fibers within the muscle in WT and CrT^{-/-} mice. **C** Representative electron micrographs of cross sections of EDL fibers from WT (left panel) and CrT^{-/-} (right panel) muscles. The intermyofibrillar space and the myofibrillar volume over the fiber volume are reported (**D**). Scale bar in (**C**): 1 μm . In (**B**) and (**D**), data are presented as mean \pm SEM. n = 15. For data analysis, parametric Student t-test (two tailed, unpaired) was used. *p < 0.05.

[Ca²⁺]_{cyt} was unaffected (Fig. 3A), caffeine-induced Ca²⁺ transients were significantly reduced in CrT^{-/-} mice compared to WT (Fig. 3B, C), suggesting either a lower amount of Ca²⁺ released from the sarcoplasmic reticulum (SR) or a reduced capacity of the mitochondrial uptake machinery. To analyze changes observed in cytosolic Ca²⁺ homeostasis, we examined whether the expression of the SR release channel RyR1 and the uptake pumps SERCA1 and SERCA2 were affected by the KO of CrT. Consistent with the reduction in cytosolic Ca²⁺ levels upon caffeine stimulation, protein levels of RyR1 are significantly reduced (Fig. 3D, E). Concurrently, SERCA2 levels, but not SERCA1 levels, are increased (Fig. 3F, G).

Mitochondria of CrT^{-/-} fibers are structurally altered, with reduced membrane potential and Ca²⁺ uptake capability

Given the well-established link between Cr and mitochondrial function [24, 28, 36], we investigated mitochondrial organization and morphology in EDL fibers of CrT^{-/-} mice at PND40. In adult EDL fibers of WT mice, mitochondria are predominantly located at the I band on both sides of the Z-line (Fig. 4A, *small arrows*) [37] are rarely found at the A-band of the sarcomere (Fig. 4A, D). These mitochondria exhibit a round or oval shape, with an average area of $60 \pm 6 \times 10^3 \text{ nm}^2$ (Fig. 4D) and display parallel cristae within a dense matrix (Fig. 4A, *inset*). They occupy about 3.5% of the total cell volume, with 8.0 ± 0.5 per 100 μm^2 of triads pairs (i.e. the Ca²⁺ release units, CRUs) (Fig. 4D). In contrast, CrT^{-/-} EDL fibers show a pronounced alteration in mitochondrial distribution. A large number of mitochondria are aligned along the A-band, forming longitudinal columns between myofibrils (Fig. 4B, *large arrow*),

with 17.5 ± 1.4 mitochondria per unit area at the A band (Fig. 4D). These mitochondria are five-time larger ($300 \pm 22 \times 10^3 \text{ nm}^2$), occupy a significantly larger fiber volume ($11.1 \pm 0.7\%$), and are less frequently associated with CRUs (5.4 ± 0.4 mitochondria per CRU pairs per unit area) (Fig. 4D). Additionally, several mitochondria display structural abnormalities, including a clear matrix and damaged internal cristae (indicated by a large black arrow in Fig. 4B, *and inset*). Moreover, damaged mitochondria frequently contain multi-layered structures (Fig. 4C, *empty arrows*), resembling lamellae arranged in a regular fashion, which may significantly alter the internal cristae organization (Fig. 4C, *dashed box and inset*). Other notable structural alterations include: i) a high incidence of fibers containing lipid droplets (Supplementary Fig. 2), which are typically absent in WT EDL fibers, and ii) about 35% of fibers showing severe damage, characterized by a total loss of cross-striation and complete disruption of the sarcomeric structure.

Mitochondrial impairment extends beyond the structural level. Specifically, by using mitochondrially targeted Fura-2/AM (mitoFura-2/AM) we found that while basal mitochondrial Ca²⁺ concentrations ([Ca²⁺]_{mt}) were comparable between WT and CrT^{-/-} FDB muscle fibers (Fig. 5A), CrT^{-/-} fibers exhibited a significant reduction in mitochondrial Ca²⁺ uptake following caffeine-induced Ca²⁺ release from the SR (Fig. 5B, C). We then investigated whether the observed Ca²⁺ phenotypes might reflect changes in the driving force of mitochondrial Ca²⁺ accumulation. To assess this, we measured mitochondrial membrane potential ($\Delta\Psi_m$) using tetramethyl rhodamine methyl ester dye (TMRM) in non-quenching mode, wherein the dye is applied at low concentrations to avoid aggregation and

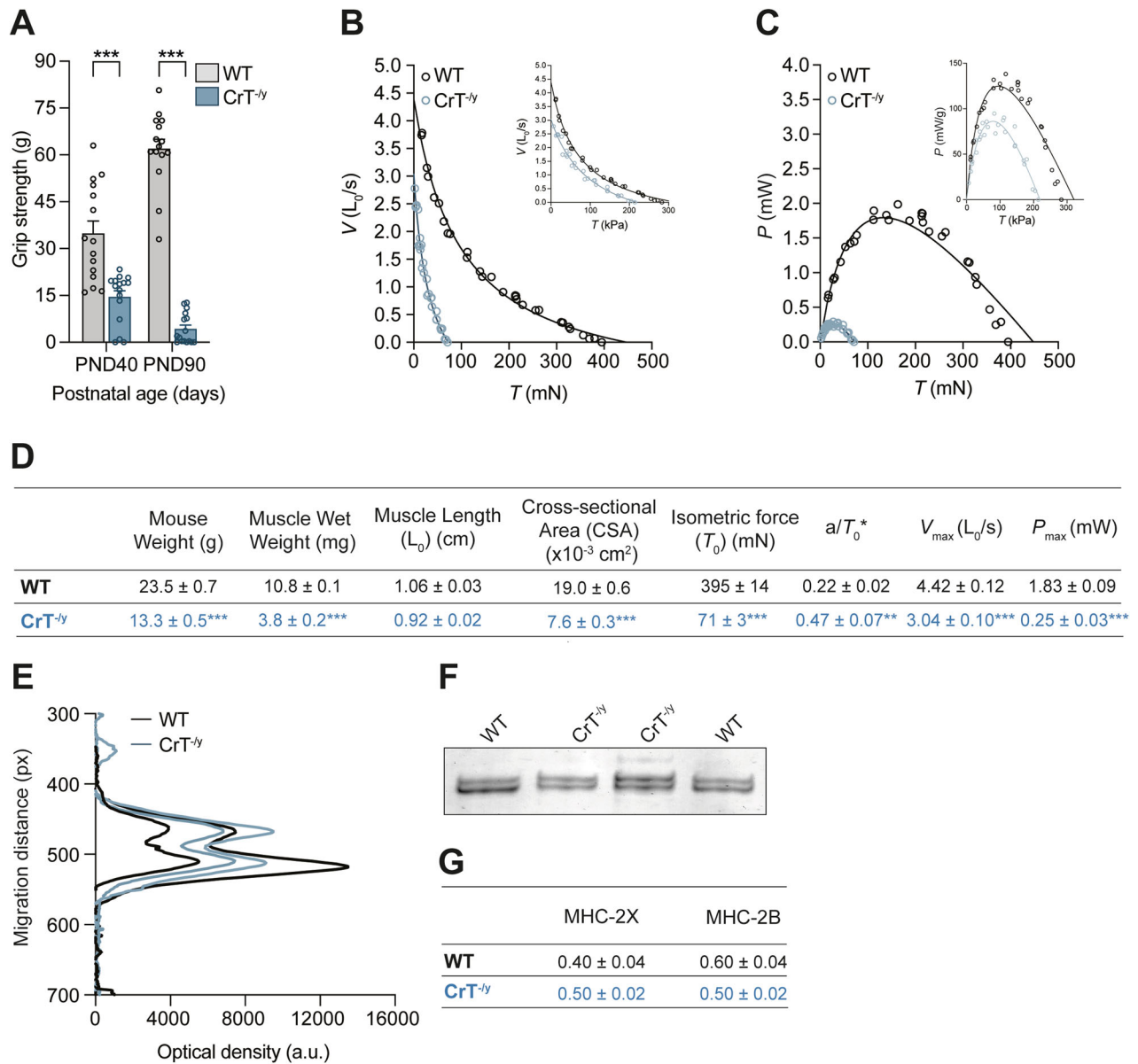
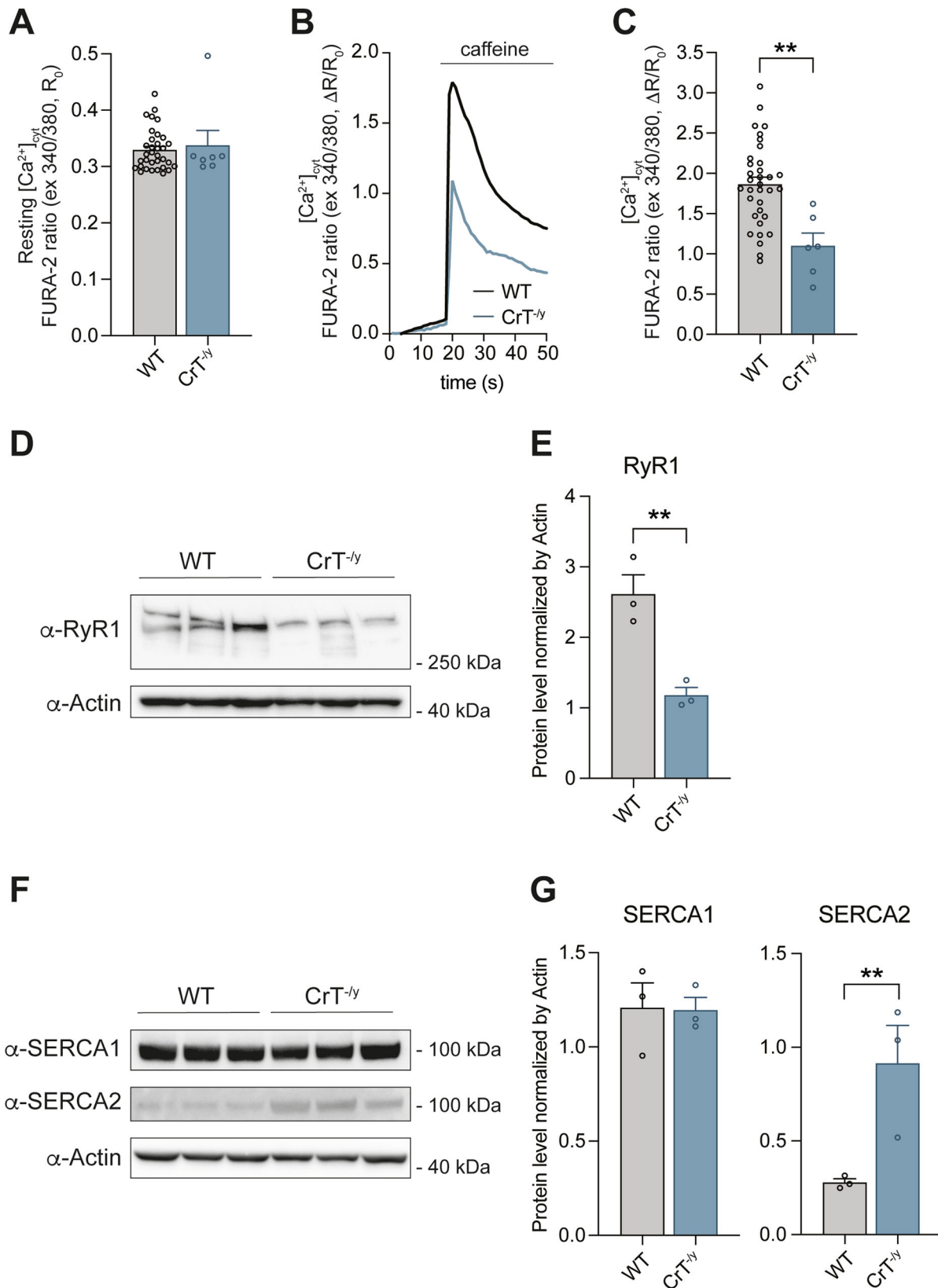


Fig. 2 **Grip strength test, force-velocity relation, power output, and myosin heavy chain expression in EDL muscles of WT and CrT $^{-/-}$ mice.** **A** Grip strength test was performed on postnatal day (PND) 40 and PND90. For data analysis, two-way ANOVA, post hoc Holm-Sidak. Data from $n = 12$. **B** Relation between force (T , mN) and shortening velocity (V , L_0/s) in WT (black symbol) and CrT $^{-/-}$ (blue symbol) mice. Lines are Hill's hyperbolic equations fit to the data (same color codes for data). Inset, same relations with force expressed in kPa after correction of the muscle CSA for the myofibrillar density in the muscle (factor α , see Text). **C** Power-force relations calculated from data (symbols) and their fits (lines) in B. Inset, same relations with force expressed in kPa after correction of CSA for the factor α . **D** Mechanical parameters during isometric contraction and during isotonic shortening of muscles from WT and CrT $^{-/-}$ mice. T_0 , maximal isometric force; a/T_0^* , is a measure of the curvature of the force-velocity relation; V_{max} , unloaded shortening velocity; P_{max} , maximum power output. T_0^* is the intercept of the Hill equation on the force-axis. In panel D, data are presented as mean \pm SEM, $n = 4$. **E** and **F** MHC isoform identification of the EDL muscle fibers by SDS-PAGE in the area of migration of the myosin heavy chains (~ 220 kDa). In (E) are shown the projections of the mass density along the vertical axis of the bands in (F) after horizontal integration. **G** Fractional expression of the MHC 2X and 2B isoforms for the WT and CrT $^{-/-}$ muscles. For data analysis, parametric Student t -test (two-tailed, unpaired) was used. * $p < 0.05$; ** $p < 0.01$; *** $p < 0.001$. Temperature 23 $^{\circ}$ C.

quenching within mitochondria. As a result, depolarized mitochondria accumulate less of the cationic dye, resulting in lower fluorescence, while hyperpolarized mitochondria show increased fluorescence due to higher dye accumulation [38]. CrT $^{-/-}$ mice showed a significant decrease in $\Delta\Psi_m$, indicating potential impairment in ATP production (Fig. 5D). As mitochondrial Ca^{2+} plays a well-established role in regulating oxidative metabolism and the $\Delta\Psi_m$ is the driving force for ATP production [39], we analyzed whether CrT $^{-/-}$ is characterized by alteration of electron transport chain. Using Western blot analysis with a Total OXPHOS Antibody Cocktail kit, targeting specific subunits of

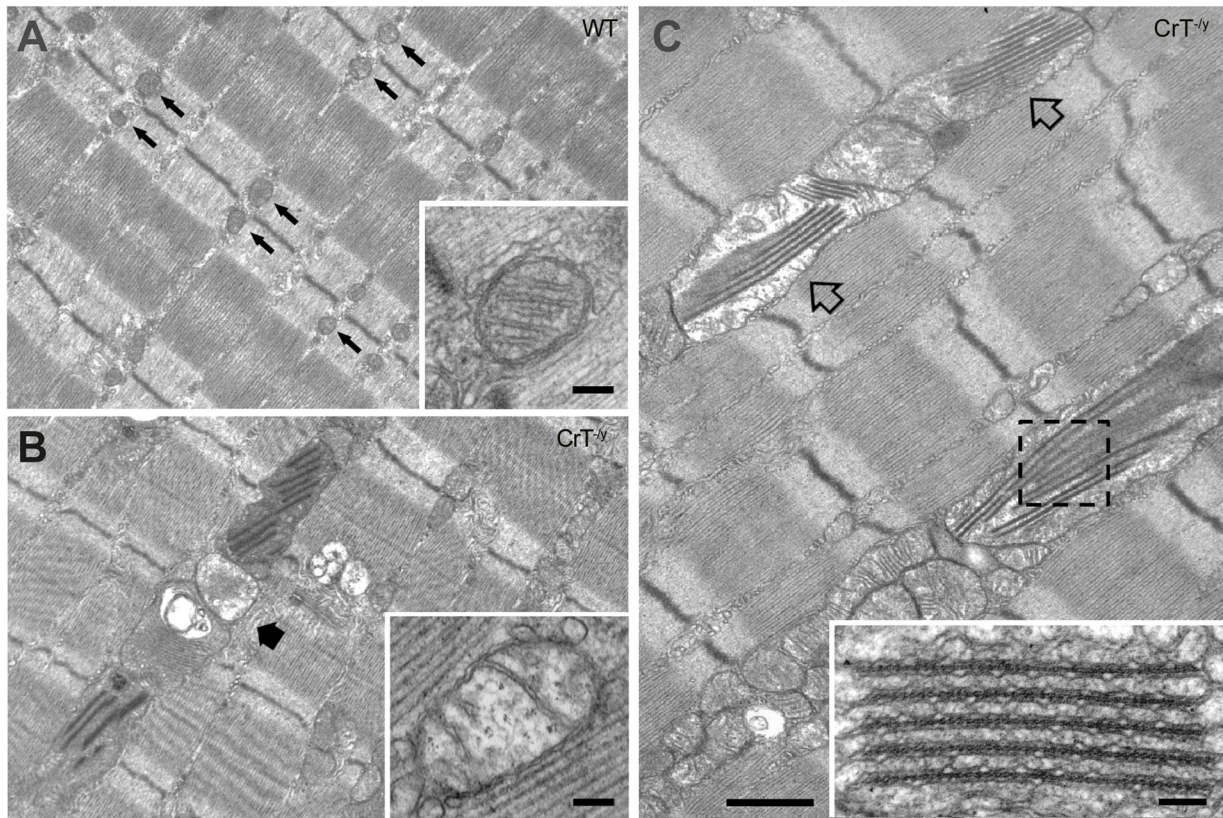
the five OXPHOS complexes (NDUFB8, SDHB, UQCRC2, MTCO1, and ATP5A), we found that CrT deletion does not reduce the protein levels of these OXPHOS subunits. Instead, a slight increase was observed in complexes V and II, indicating the possible activation of potential compensatory mechanisms (Fig. 5E). Further analysis of ATP production in muscle tissue, indeed, showed that CrT deletion leads to a significant reduction in ATP levels (Fig. 5F), supporting an overall impairment in mitochondrial function in CrT $^{-/-}$ muscles. Given the reduced mitochondrial Ca^{2+} entry, we investigated the expression of the different components of the Mitochondrial Calcium Uniporter



(MCU) complex, the channel responsible for Ca^{2+} entry into mitochondria. Our results revealed a significant increase in the mRNA expression of the crucial regulator of the channel MICU1 (Fig. 5G), as well as elevated protein levels of both the pore-forming subunit MCU

and MICU1 in CrT^{-ly} mice compared to WT (Fig. 5H). To explore the discrepancy between reduced mitochondrial Ca^{2+} uptake and increased expression of MCU complex components, we measured Ca^{2+} extrusion rates in WT and CrT^{-ly} muscles. We found no

Fig. 3 Characterization of cytosolic Ca^{2+} homeostasis in FDB fibers of WT and $\text{CrT}^{-/-}$ mice. WT and $\text{CrT}^{-/-}$ myofibers were loaded with cytosolic Fura-2/AM. **A** Resting cytosolic Ca^{2+} concentrations; **B** representative traces of cytosolic Ca^{2+} concentrations upon caffeine stimulation; **C** cytosolic Ca^{2+} concentrations upon caffeine stimulation. Data are presented as mean \pm SEM. $n > 20$. For data analysis, parametric Student *t*-test (two-tailed, unpaired) was used. ****** $p < 0.01$. **D** Representative Western blot of WT and $\text{CrT}^{-/-}$ TA muscles stained with α -RyR1 antibody. α -Actin was used as loading controls. $n = 3$. **E** Quantification of the immunoblots showed in D. The levels of the protein were normalized by actin levels. Data are presented as mean \pm SEM. $n = 3$. For data analysis, parametric Student *t*-test (two-tailed, unpaired) was used. ****** $p < 0.01$. **F** Representative Western blot of WT and $\text{CrT}^{-/-}$ TA muscles stained with α -SERCA1 and α -SERCA2 antibodies. α -Actin was used as loading controls. $n = 3$. **G** Quantification of the immunoblots showed in D. The levels of the protein were normalized by actin levels. Data are presented as mean \pm SEM. $n = 3$. For data analysis, parametric Student *t*-test (two-tailed, unpaired) was used. ****** $p < 0.01$.



D

	Mitochondrial volume/total volume (%)	No. of mitochondria/100 μm^2	No. of mitochondria at the A band/100 μm^2	No. of mitochondria/CRU pairs/100 μm^2	Size of apparently normal mitochondria ($\text{nm}^2 \times 10^3$)
WT	3.5 \pm 0.3	29.6 \pm 1.8	1.2 \pm 0.3	8.0 \pm 0.5	60 \pm 6
$\text{CrT}^{-/-}$	11.1 \pm 0.7*	35.2 \pm 2.1*	17.5 \pm 1.4*	5.4 \pm 0.4*	300 \pm 22

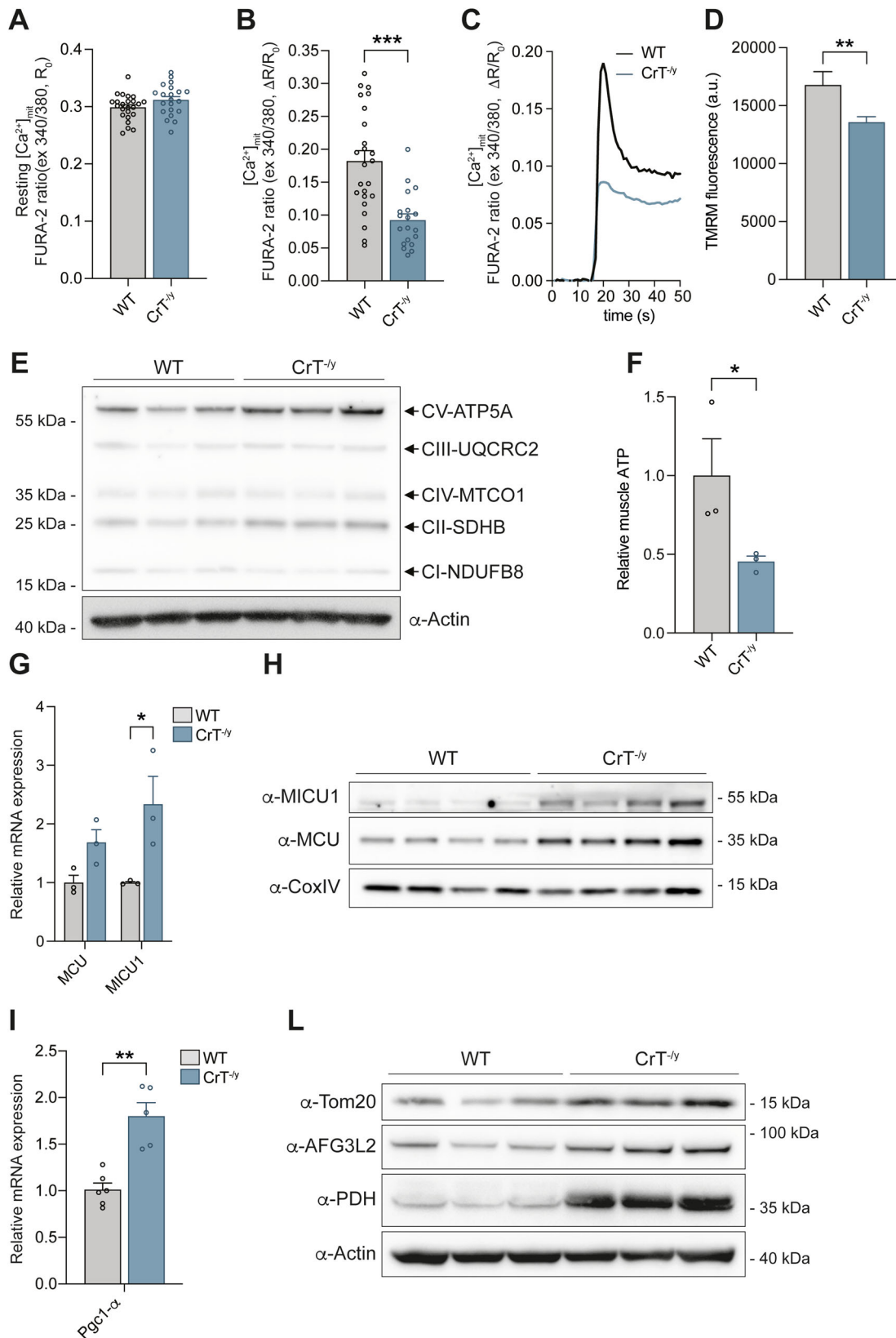
Fig. 4 $\text{CrT}^{-/-}$ mitochondria present morphological abnormality. Representative electron microscopy pictures of EDL muscle fibers in control (A) and $\text{CrT}^{-/-}$ mice (B) and (C). Scale bars: 1 μm (insets: 0.1 μm). **D** Quantitative EM analysis. Data are presented as mean \pm SEM. Sample size: 15 fibers from 1 WT mice, 30 fibers from 2 CK-KO mice; 5 micrographs/fiber. For data analysis, parametric Student *t*-test (two-tailed, unpaired) was used. ***** $p < 0.05$.

significant differences between the two groups (Supplementary Fig. 3). Furthermore, analysis of the mRNA expression of the *Pgc1- α* gene showed that the lack of CrT triggers the induction of *Pgc1- α* (Fig. 5I), indicating enhanced mitochondrial biogenesis, which aligns with our ultrastructural findings (Fig. 4) and the increased expression of MCU complex subunits. We also analyzed the protein expression of key mitochondrial markers from distinct compartments: Tom20 (outer membrane), AFG3L2 (inner membrane), and PDH (matrix). The expression levels of all these proteins were elevated in $\text{CrT}^{-/-}$ muscles compared to WT (Fig. 5L and Supplementary Fig. 4), further corroborating our previous findings of mitochondrial alterations. In

summary, these findings suggest that CrT deficiency in skeletal muscle leads to compromised mitochondrial Ca^{2+} homeostasis, which may contribute to the observed pathological phenotype.

The IGF-1/Akt/PKB pathway is suppressed and the expression of atrophy-specific E3 ubiquitin ligases is induced in $\text{CrT}^{-/-}$ mice

To elucidate the mechanism underlying the atrophic phenotype in $\text{CrT}^{-/-}$ animals, we directed our focus toward the established hypertrophy pathways in skeletal muscle, specifically the IGF1-Akt/PKB signaling axis [40]. This pathway is crucial for promoting



muscle hypertrophy, whereas its suppression is known to lead to muscle atrophy [40]. In CrT^{-ly} animals, we observed a marked suppression of Akt signaling, as evidenced by reduced phosphorylation of Akt, S6, and 4E-BP1 (Fig. 6A–D). These findings suggest

that the atrophic phenotype in CrT^{-ly} mice is likely due to impaired IGF1/Akt/PKB signaling. Additionally, we noted a significant upregulation of Atrogin-1 and MUSA1, two E3 ubiquitin ligases known to be involved in protein degradation during

Fig. 5 Mitochondrial Ca^{2+} uptake and membrane potential are decreased in $\text{CrT}^{-/y}$ muscles compared to WT and the mRNA and protein expression of crucial components of the MCU complex is elevated. WT and $\text{CrT}^{-/y}$ myofibers were loaded with mitochondrially targeted Fura-2/AM (mitoFura-2/AM). **A** Resting mitochondrial Ca^{2+} concentrations are unaltered in $\text{CrT}^{-/y}$ myofibers compared to WT. **B** Ratiometric measurements of mitochondrial Ca^{2+} uptake upon caffeine treatment in $\text{CrT}^{-/y}$ FDB myofibers compared to WT fibers. **C** Representative traces of the experiment. Data are presented as means \pm SEM. $n > 20$. For data analysis, parametric Student *t*-test (two-tailed, unpaired) was used. $***p < 0.001$. **D** TMRM fluorescence in FDB fibers of WT and $\text{CrT}^{-/y}$ mice. Data are presented as mean \pm SEM. $n = 20$. For data analysis, parametric Student *t*-test (two-tailed, unpaired) was used. $**p < 0.01$. **E** Representative Western blot of the OXPHOS complexes in WT and $\text{CrT}^{-/y}$ muscles. $n = 3$. **F** Relative skeletal muscle ATP levels in EDL muscles of WT and $\text{CrT}^{-/y}$ muscles. $n = 3$. For data analysis, parametric Student *t*-test (two-tailed, unpaired) was used. $*p < 0.05$. **G** Real-time RT-PCR analyses of WT and $\text{CrT}^{-/y}$ muscles with the indicated oligonucleotide primers. Data are presented as mean \pm SEM. $n = 3$. For data analysis, parametric Student *t*-test (two-tailed, unpaired) was used. $*p < 0.05$. **H** Representative Western blot of WT and $\text{CrT}^{-/y}$ EDL muscles. α -CoxIV was used as loading control. $n = 4$. **I** Real-time RT-PCR analyses of WT and $\text{CrT}^{-/y}$ muscles with the indicated oligonucleotide primers. Data are presented as mean \pm SEM. $n = 5$. For data analysis, parametric Student *t*-test (two-tailed, unpaired) was used. $**p < 0.01$. **L** Representative Western blot of WT and $\text{CrT}^{-/y}$ TA muscles stained with α -Tom20, α -AFG3L2 and α -PHD antibodies. α -Actin was used as loading controls. $n = 3$.

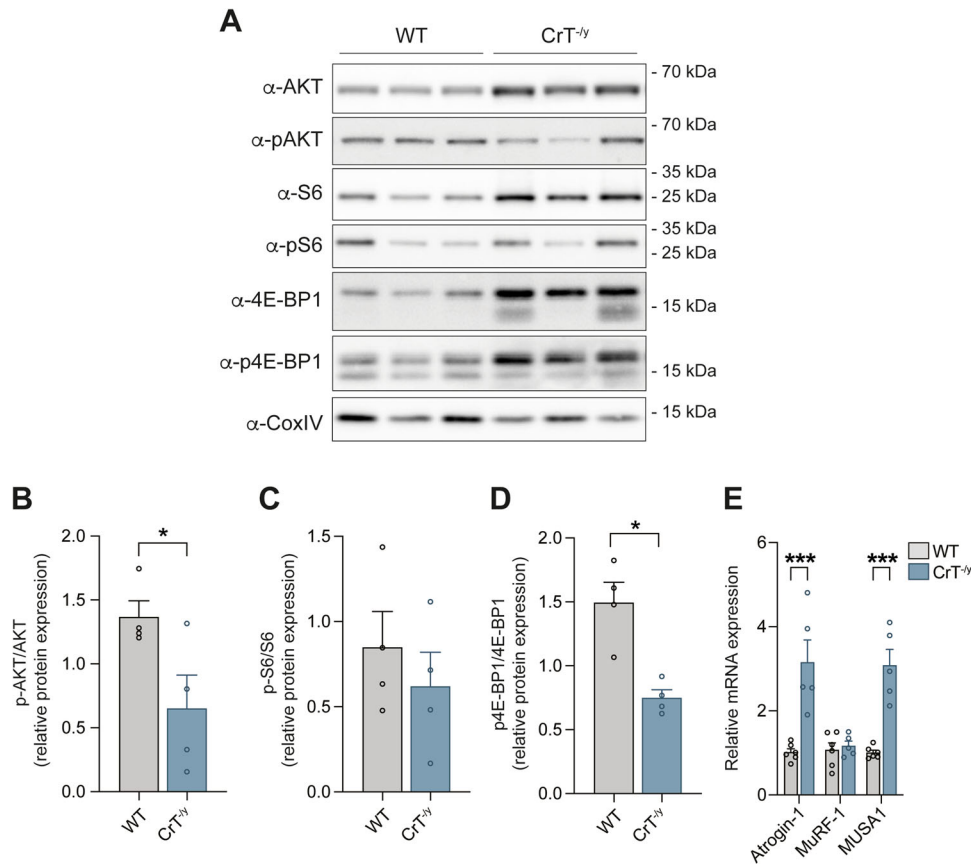


Fig. 6 The lack of CrT induces mitochondriogenesis and specific atrophy programs. **A** Representative Western blot of WT and $\text{CrT}^{-/y}$ EDL muscles stained with the indicated antibodies. α -CoxIV was used as loading control. $n = 3$. **B–D** Quantification of the experiment performed as in (A). Data are presented as mean \pm SEM. $n = 4$. For data analysis, parametric Student *t*-test (two-tailed, unpaired) was used. $*p < 0.05$. **E** Real-time RT-PCR analyses of WT and $\text{CrT}^{-/y}$ muscles with the indicated oligonucleotide primers. Data are presented as mean \pm SEM. $n = 5$. For data analysis, parametric Student *t*-test (two-tailed, unpaired) was used. $***p < 0.001$.

muscle atrophy [40] (Fig. 6E). This increased expression further supports the association between CrT deficiency and enhanced muscle atrophy through disrupted signaling pathways and elevated protein degradation.

DISCUSSION

Creatine (Cr) is essential for supplying cells with high-energy phosphates, facilitating the rapid regeneration of hydrolyzed ATP. The creatine transporter (CrT/SLC6A8) is crucial for transporting Cr across tissue barriers and into specific cells, such as neurons and myocytes [41]. Mutations in the CrT gene lead to Creatine Transporter Deficiency (CTD), associated with severe intellectual disability, epilepsy, autism, developmental delay, and motor

dysfunction [8, 41]. While these manifestations primarily impact brain function, non-neurological symptoms, including gastrointestinal dysfunction, bladder dysfunction, cardiomyopathy, and ophthalmologic abnormalities, are also observed [11, 12]. Skeletal muscle hypotonia and nonspecific myopathic symptoms are common, though the literature on muscle Cr levels in CTD patients is poor [13, 17, 18]. Despite the limited understanding of peripheral contributions to CTD pathology, evidence suggests that muscle impairment could affect neurological symptoms, as brain-specific $\text{CrT}^{-/y}$ mice do not fully reproduce the early pathological features or autistic traits of CTD patients [42].

To address the gap in understanding muscle phenotype, we characterized the skeletal muscle of the $\text{CrT}^{-/y}$ mouse model, which exhibits reduced body weight and cognitive impairments

similar to those observed in CTD patients [23]. Creatine levels in the skeletal muscle of these mice were dramatically reduced (~65% at PND30 and ~95% in adults, [23]), with insufficient compensation from increased AGAT expression [21, 43]. Our data clearly show that CrT^{-/-} muscles are dramatically atrophic (Fig. 1A, B) in accordance with previous results [21, 25]. Additionally, in EDL muscles the proportion of contractile elements in terms of fiber volume is significantly diminished in CrT^{-/-} muscles compared to WT, leading to a consequent increase of the intermyofibrillar space (Fig. 1C, D). This observation supports the atrophic phenotype of this murine model. Fiber atrophy in CrT^{-/-} muscles is associated to a functional decline, characterized by reduced grip strength, both at PND 40 and 90, with a marked reduction in isometric force and power at PND 40 (Fig. 2A–C).

In WT mouse, with a CSA of the EDL muscle of $19 \times 10^{-3} \text{ cm}^2$ (Fig. 2D), the specific isometric force per unit area is ($395 \text{ mN} / 19 \times 10^{-3} \text{ cm}^2 =$) $208 \pm 10 \text{ kPa}$. As the muscle fibers represent 87% of the cross-sectional area and the area of the fiber occupied by the myofibrils is 84.5% (Fig. 1B), the CSA occupied by the myofibrils is $\alpha = 74\%$ of the muscle CSA, and T_0 is ($395 \text{ mN} / (19 \times 10^{-3} \text{ cm}^2 \times \alpha) =$) $281 \pm 10 \text{ kPa}$. In CrT^{-/-} mouse, with a muscle CSA = $7.6 \times 10^{-3} \text{ cm}^2$ (Fig. 2D) and $\alpha = 44\%$ (muscle fibers occupy 62% of the muscle CSA; myofibrils occupy 71% of the fiber CSA, Fig. 1B), the same calculation gives an isometric force of $212 \pm 17 \text{ kPa}$, about 30% lower than in WT mouse. After correction, the maximum power developed by the myofibrils within the muscle is about 35% lower in CrT^{-/-} mouse ($82 \pm 2 \text{ mW/g}$) than in control ($128 \pm 2 \text{ mW/g}$) (Inset Fig. 2C). The reduced power in CrT^{-/-} mice cannot be explained by differences in mechanical parameters resulting from the shift in myosin heavy chain isoforms (Supplementary Fig. 1C). Instead, it may be related to the disruption of sarcomere structure observed in some fibers (Supplementary Fig. 2), a decreased cytosolic $[\text{Ca}^{2+}]$ in response to caffeine (Fig. 3B, C), reduced Ca^{2+} release from the ER, as indicated by the lower protein levels of RyR1 (Fig. 3D, E), and an increased capacity of the SR to reuptake Ca^{2+} upon stimulation, evidenced by elevated SERCA2 protein levels (Fig. 3F, G). Furthermore, in addition to the shift from the faster MHC-2B isoform to the slower MHC-2X isoform, the presence of disrupted sarcomeres behaving as passive elements could also generate an internal load and contribute to the reduction of the shortening velocity more evident at low loads.

Cytoarchitectural abnormalities and a higher proportion of the cell volume occupied by mitochondria, resulting in a decreased concentration of myofibrils, have been observed in other models of creatine deficiency [27, 28, 44] and an increase in $[\text{Ca}^{2+}]_{\text{cyt}}$ occurs only during repeated tetanic stimulation, accompanied by a significant decline in force in CK knockout mouse fibers [26].

The structural analysis of the current study has been focused on EDL muscles. EDLs are mostly composed of type IIb (fast-twitch glycolytic) fibers which rely mainly on glycogen for anaerobic metabolism. Contrary to type I (slow-twitch oxidative) fibers, which have normally a high content of lipid droplets and mitochondria as their energy metabolism is completely aerobic, type IIb fibers have reduced mitochondrial volume and lower contents of lipid droplets [45]. The structural observations and the quantitative analysis revealed that in EDL fibers from CrT^{-/-} mice there is an increase in mitochondrial number/volume and size (Fig. 4D), accompanied by a corresponding increase in the protein expression levels of mitochondrial outer and inner membrane and matrix proteins (Fig. 5L and Supplementary Fig. 4). In addition, in CrT^{-/-} fibers a high percentage of mitochondria is placed at the A-band of the sarcomere, a spatial characteristic disposition of slow-twitch fibers (Fig. 4D). Interestingly, an unusual high number of lipid droplets, which are usually not present in WT EDL fibers, has been also observed (Supplementary Fig. 2). A similar phenomenon has been documented in the AGAT^{-/-} model of creatine deficiency [28]. In this model, the increased activity of

citrate synthase and F-type ATPase, along with the presence of intramyocellular lipid droplets, indicates a boost in oxidative ATP production within the mitochondria of resting AGAT^{-/-} muscle [28].

These structural results significantly support the change in the fiber composition and/or metabolism, with a fiber-type shift towards a slower isoform (Fig. 2E–G), induced by the absence of CrT.

In CrT^{-/-} mice, the increased mitochondrial volume is accompanied by elevated expression of the master regulator of mitochondrial biogenesis, PGC-1 α (Fig. 5I), suggesting that creatine deficiency in skeletal muscle induces a precise transcriptional program. This result not only supports the increase in both the quantity and size of mitochondria (Figs. 4, 5L and Supplementary Fig. 4) but also accounts for the slower myosin heavy chain phenotype (Fig. 2F). Indeed, this transcriptional co-activator, working in conjunction with Mef2, activates transcription and acts as a target for calcineurin signaling, a pathway implicated in the expression of genes associated with slow fibers [46]. Overexpression of PGC-1 α in skeletal muscle has been shown to induce angiogenesis, improve muscle endurance, motor coordination, and balance in aged animals, and activate mitochondrial oxidative metabolism [46]. Hence, the elevated expression of PGC-1 α in CrT^{-/-} may also serve as a compensatory mechanism activated to mitigate atrophy.

Numerous mitochondria in EDL CrT^{-/-} fibers showed a very peculiar structural arrangement of internal cristae resembling multi-layered crystal-like structure rows (Fig. 4C, empty arrows). These structures were previously reported in the AGAT^{-/-} model of creatine deficiency [40], but up today either assembling or function is unknown. However, a comprehensive assessment of this issue extends beyond the scope of the current study.

Mitochondrial alterations extend beyond structure to function. Indeed, we observed a significant reduction in $\Delta\Psi_m$ (Fig. 5D) and a marked decrease in Ca^{2+} influx into the mitochondria in isolated fibers of the FDB CrT^{-/-} muscle stimulated with caffeine (Fig. 5B, C). Notably, we did not observe any changes in the quantification of Ca^{2+} under basal conditions (Fig. 5A). Although the protein expression levels of some of the components of the respiratory chain complexes were not reduced but rather induced in CrT^{-/-} muscles compared to WT (Fig. 5E), ATP production is significantly decreased (Fig. 5F). This result aligns with the crucial role of mitochondrial Ca^{2+} in controlling the rate of ATP generation within mitochondria [39].

It is also possible that the observed reduction in mitochondrial Ca^{2+} uptake in isolated fibers of the FDB from CrT^{-/-} mice could at least in part be due to the reduction in the number of CRU-mitochondrial pairs/100 μm^2 (Fig. 4D) as previously reported in ageing [47] and in SEP1N-related myopathy patients [48, 49].

Specifically, changes in the relationship between mitochondria and CRUs may contribute to impaired delivering of sufficient levels of Ca^{2+} and ATP required for optimal force generation and muscle performance. Data presented here in EDL from CrT^{-/-} mice focus attention on previously unreported alterations not only in mitochondrial morphology but also in their position and orientation with respect to the sarcomeric structure. In EDL fibers from CrT^{-/-} mice, a significantly higher percentage of mitochondria are longitudinally oriented along the A band, rather than occupying their normal I band position (Fig. 4D) and this structural result may likely account for the observed significant reduction (about 35%) in the number of CRU-mitochondria pairs, a factor which could significantly interfere with a proper Ca^{2+} uptake and ATP production.

The decrease in mitochondrial Ca^{2+} is paradoxically accompanied by an elevation in the expression of the pore-forming subunit of the channel responsible for mitochondrial Ca^{2+} entry, MCU, and its positive regulator MICU1 (Fig. 5G, H). This increase, which we have shown to be independent of increased Ca^{2+}

extrusion rates from mitochondria (Supplementary Fig. 3), may result from both an expansion of mitochondrial volume and either modifications to other channels (e.g., post-translational modifications) or changes in the expression of other MCU subunits.

We extensively demonstrated that mitochondrial Ca^{2+} entry controls muscle homeostasis [50, 51]. Indeed, silencing MCU triggers muscle atrophy, while its overexpression leads to muscle hypertrophy [51]. In relation to the mechanism, mitochondrial Ca^{2+} uptake regulates skeletal muscle trophism by modulating the IGF-1-AKT/PKB and the PGC-1 α pathways [51]. Based on these premises, we asked whether signaling pathways controlling muscle homeostasis were altered in CrT^{-/-} animals focusing our attention on the IGF-1/AKT/mTOR pathway, whose activation induces skeletal muscle hypertrophy by stimulating protein translation and concomitantly suppressing protein breakdown by phosphorylating the transcription factor FoxO3 [40]. In line with the marked reduction of the muscle CSA, we found that the phosphorylation levels of AKT and of its downstream target 4E-BP1 are inhibited in EDL muscles of CrT KO mice (Fig. 6A–D). Consistently, the expression of the ubiquitin ligases Atrogin-1 and MUSA1, involved in protein degradation during muscle atrophy [40], are induced (Fig. 6E). The suppression of the IGF-1/Akt/PKB pathway and induction of atrophy-specific E3 ubiquitin ligases, such as Atrogin-1 and MUSA1, further support the link between creatine deficiency and muscle atrophy. While the total knockout model does not differentiate between neuronal and muscular contributions, it is likely that reduced creatine levels in skeletal muscle could impact muscle function, especially under stress conditions like intense exercise or infections.

While employing a total KO model prevents a clear distinction between neuronal and muscular contributions to motor function, and impaired skeletal muscle function may not be a predominant symptom in most CrT-deficient patients, we suggest that diminished creatine levels in skeletal muscle could potentially compromise muscle function, particularly under stress conditions like intense exercise or infections in these patients.

In summary, our findings demonstrate that muscles in CrT^{-/-} mice display significant morphological and functional abnormalities, culminating in a pronounced atrophic phenotype with substantially reduced performance at intermediate-high loads and limited shortening capability at low loads. These findings underscore the role of Cr deficiency in muscle pathology and suggest that muscle impairment may contribute to the overall disease phenotype in CTD. Notably, heterozygous females were not investigated in this study, leaving open questions about whether similar but potentially less severe phenotypes occur in female carriers.

MATERIALS AND METHODS

Animals

We employed male mice hemizygous for the deletion of exons 5–7 in the *Slc6a8* gene (KO; CrT^{-/-}) and their wild-type (WT; CrT^{+/-}) littermates [20]. Animals were raised or acclimatized to the conditions of the animal facility, and housed in a ventilated room under a controlled temperature (21 ± 2 °C), with a 12:12 h light:dark cycle and free access to chow rodent diet and water *ad libitum*.

Light microscopy

For histological examination by light microscopy (LM) semithin sections (~700 nm) were cut using a Leica Ultracut R microtome (Leica Microsystems, Vienna, Austria) with a Diatome diamond knife (Diatome, Biel, Switzerland) and were stained in a solution containing 1% toluidine blue O and 1% sodium borate (tetra) in distilled water for 3 min on a hot plate at 55–60 °C. After washing and drying, sections were mounted with DPX media for histology (Sigma–Aldrich, Milan, Italy) and observed with a Leica DMLB light microscope connected to a DFC450 camera equipped with Application Suite v 4.13.0 for Windows (Leica Microsystems, CMS GmbH, Switzerland).

Electron microscopy

EDL muscles were dissected from mice, fixed at room temperature with 3.5% glutaraldehyde in 0.1 M NaCaCo buffer (pH 7.2), and kept at 4 °C in fixative until further use. Fixed muscles were then post-fixed, embedded, stained en-block, and sectioned for EM, as described previously [37]. For EM, ultrathin sections (~50 nm), were examined after staining in 4% uranyl acetate and lead citrate, with a Morgagni Series 268D electron microscope (FEI Company, Brno, Czech Republic), equipped with Megaview III digital camera (Munster Germany) at 60 kV.

EM quantitative analysis

Estimates of the relative fiber volume occupied by myofibrils were calculated in transversal sections by the well-established stereology point counting technique [52, 53]. Briefly, 2 micrographs from each fiber (sample size: 15 fibers for each group) were taken at a magnification of 22 K excluding nuclei and subsarcolemmal regions. A grid of an orthogonal array of dots at a spacing of 0.35 μm was superimposed on each micrograph. The relative fiber volume occupied by the myofibrils vs. intermyofibrillar elements was then calculated by dividing the total number of dots by the number of dots falling in either one of the compartments.

Behavioral testing

In the grip strength test, a peak amplifier is used to automatically measure the maximum force exerted by the animal's forelimbs [54].

Muscle mechanical analyses

EDL muscle from WT or CrT^{-/-} mice (PND40) was dissected under a stereomicroscope and mounted horizontally between the lever of a motor/force transducer system (305C, Aurora Scientific Inc.) and a lever carried by a micromanipulator in a trough, containing physiological Krebs–Henseleit solution (composition (mM): 119 NaCl, 4.7 KCl, 1.0 MgSO₄, 25 NaHCO₃, 1.2 KH₂PO₄, and 1.1 glucose), continuously saturated with carbogen (95% O₂ and 5% CO₂, pH 7.4) at room temperature (22–24 °C). The muscle was straightened just above its slack length using the micromanipulator. The trough was sealed with a Perspex cover and mounted vertically on the stage with the motor/force transducer system on the top. Trains of stimuli of alternate polarity to elicit fused tetani (frequency 100–120 Hz) were delivered by means of two platinum wire electrodes running parallel to the muscle, 1 cm apart. The intensity of the stimuli was increased until the isometric plateau force reached a maximum constant value, T_0 (indicating that all cells in the muscle were activated). Muscle length was further finely adjusted using the micromanipulator to obtain the maximum isometric force corresponding to the plateau of the force–length relation. Isometric force was normalized to muscle Cross-Sectional Area (CSA), calculated from the muscle wet weight (w) according to the relation: $\text{CSA} = (w \cdot \cos\theta) / (L_f \cdot \delta)$, where θ is the pennation angle of the fibers (8.3°, [55]), L_f is the fiber length (cm), and δ is the muscle density, 1.056 g/cm³ [56]. L_f was obtained by multiplying the muscle length by 0.51 [55]. The force–velocity relation was determined by measuring the velocity of steady shortening (V) after a drop in force from T_0 to a preset value $T < T_0$ (see Supplementary Fig. 1A for the protocol). The force–velocity points were fitted to the Hill hyperbolic equation [56]: $(T + a)(V + b) = (V_0 + b)a$, where a , b , and V_0 (unloaded shortening velocity) are the regression parameters. Force and motor positions were recorded with a multifunction I/O board (PCI-6110E, National Instruments), and a dedicated program written in LabView (National Instruments) was used for signal recording and analysis.

RNA extraction, reverse transcription, and quantitative real-time PCR (RT-PCR). Total RNA was extracted from EDL muscles using Trizol reagent, following the manufacturer's instructions. The RNA was quantified using a Nanodrop spectrophotometer (Thermo Fisher Scientific). Complementary DNA (cDNA) was synthesized from 300 ng of total RNA using the SuperScript II cDNA Synthesis Kit with oligo(dT)_{12–18} primers for first-strand synthesis by reverse transcriptase. The cDNA was analyzed by quantitative real-time PCR (RT-PCR) on an IQ5 thermocycler using SYBR Green chemistry (Bio-Rad). Expression levels were quantified using the 2- $\Delta\Delta\text{CT}$ method [57].

Real-time PCR primer sequences were as follows:

MCU: FW AAAGGAGCCAAAAGTCACG RV AACGGCGTGAGTTACAAACA
 MICU1: FW AAGGCAGCATCTTACAGCC RV CCTGCTCAAACCTCCTCATGT
 PGC-1 α : FW CGCTGCTCTTGAGAATGGAT RV CGCAAGCTTCTGAGCTTC
 ACTIN: FW CTGGGCTCTAGCACCATGAAGAT RV GGTGGACAGTGAGGCC

AGGAT ATROGIN-1: FW GCAAACACTGCCACATTCTCTC RV CTTGAGGGG
 AAAGTGAGACG MUSA1: FW TCGTGGAATGGTAATCTTGC RV CCTCCCGT
 TTCTCTATCACG MURF1: FW CTTCTCTCAAGTGCCAAG RV CCTCAAGGC
 CTCTGCTATGT.

Raw data are included as Supplemental Material.

Western blotting and antibodies. Frozen muscles were pulverized using the QIAGEN Tissue Lyser for protein extraction. The protein lysis buffer used contained 50 mM Tris pH=7.5, 150 mM NaCl, 5 mM MgCl₂, 1 mM DTT, 10% glycerol, 2% SDS, 1% Triton X-100, Roche Complete Protease Inhibitor Cocktail, 1 mM PMSF, 1 mM NaVO₃, 5 mM NaF and 3 mM β-glycerophosphate. A total of 40 μg of protein, quantified using the BCA assay, was loaded onto 4–12% acrylamide gels for SDS-PAGE. Proteins were separated by SDS-PAGE and transferred onto nitrocellulose membranes using the semi-dry method. Blots were blocked for 1 h at room temperature with 5% non-fat dry milk in TBS-T buffer (50 mM Tris, 150 mM NaCl, and 0.01% Tween.20, pH = 7.4) and then incubated at 4 °C with primary antibodies overnight. Secondary antibodies were applied for 1 h at room temperature. The following primary antibodies, used at dilution 1:1000, were used: COX IV (Cell Signaling Technology, Cat #4844), MCU (Merck, Cat #HPA016480), MICU1 (Merck, Cat #HPA037479), Akt (pan) (C67E7) (Cell Signaling Technology, Cat #46915), Phospho-Akt (Ser473) (D9E) (Cell Signaling Technology, Cat #40605), S6 ribosomal protein (5G10) (Cell Signaling Technology, Cat #2217), Phospho-S6 (S240/244)XP (Cell Signaling Technology, Cat #5364), 4EBP1 (Cell Signaling Technology, #9452), phospho-4EBP1 (Thr37/46) (Cell Signaling Technology, Cat #9459), Actin (Merk, Cat # A4700), SERCA1 (Thermo Fisher Scientific, Cat # MA3-911), SERCA2 (Thermo Fisher Scientific, Cat # 2A7-A1), AFG3L2 (Thermo Fisher Scientific, Cat # PA5-95347), TOM20 (Cell Signaling Technology, Cat #42406), PDH (Cell Signaling Technology, Cat #2784), Total-OXPHOS (Abcam, Cat # ab110413).

Full-length uncropped original western blots used in the manuscript are included as Supplemental Material.

FDB fiber dissociation and culture. FDB fibers were isolated from muscle digested in collagenase A (4 mg/mL) (Roche) dissolved in Tyrode's salt solution pH = 7.4, containing 10% FBS. Single fibers were obtained by mechanical dissociation and plated on laminin-coated glass coverslips. The FDB fibers were cultured in DMEM with HEPES, supplemented with 10% FBS, containing penicillin (100 U/mL) and streptomycin (100 U/mL), at 37 °C with 5% CO₂.

Cytosolic and mitochondrial [Ca²⁺] measurements in FDB fibers. For cytosolic [Ca²⁺] measurements, FDB fibers were loaded with 2 μM cytosolic Fura-2/AM (Thermo Fischer Scientific, #F1221) diluted in Krebs-Ringer modified buffer (135 mM NaCl, 5 mM KCl, 1 mM MgCl₂, 20 mM HEPES, 1 mM MgSO₄, 0.4 mM KH₂PO₄, 1 mM CaCl₂, 5.5 mM glucose, pH = 7.4), containing 0.02% Pluronic acid for 20 min and then washed with Krebs-Ringer modified buffer in the presence of 75 μM N-benzyl-P-toluenesulfonamide (BTS) to avoid fiber contraction. Ca²⁺ release from the ER was induced with 20 μM caffeine treatment.

For mitochondrial [Ca²⁺] measurements, FDB fibers were loaded with 2 μM mitochondrially targeted mitoFURA-2/AM [58] diluted in Krebs-Ringer modified buffer (described above) containing 0.02% Pluronic acid for 30 min and then washed with Krebs-Ringer modified buffer in the presence of 75 μM BTS. Ca²⁺ release from the ER was induced with 20 μM caffeine treatment.

Cytosolic and Mitochondrial [Ca²⁺] experiments were performed on a Zeiss Axiovert 200 microscope equipped with a 40x/1.3 N.A. PlanFluor objective. Excitation was performed with a DeltaRAM V high-speed monochromator (Photon Technology International) equipped with a 75 W xenon arc lamp. Images were captured with a high-sensitivity Evolve 512 Delta EMCCD (Photometrics). The system was controlled by MetaMorph 7.5 (Molecular Devices) and was assembled by Crisel Instruments. Images were collected by alternatively exciting the fluorophore at 340 and 380 nm and fluorescence emission was recorded through a 515/30 nm band-pass filter (Semrock). Image analysis was performed with Fiji distribution of the ImageJ software. The images analyzed were background subtracted.

Mitochondrial Ca²⁺ efflux was normalized on the maximum Ca²⁺ value after caffeine stimulation.

Mitochondrial membrane potential. Isolated FDB muscle fibers were incubated with 20 nM tetramethyl rhodamine methyl ester dye (TMRM) in non-quenching mode together with 75 μM BTS in Krebs-Ringer modified buffer for 20 min at 37 °C. In non-quenching mode, the probe is used at lower concentrations to avoid dye aggregation and quenching within

mitochondria. Consequently, depolarized mitochondria will accumulate less of the cationic dye and display reduced fluorescence, whereas hyperpolarised mitochondria will accumulate more dye, resulting in higher fluorescence [38]. Data acquisition was done with Leica TCS-SP5-II equipped with a PlanApo 100x/1.4 N.A. objective. The TMRM fluorescence was excited by the 543 nm HeNe laser, and its emission was collected in the 555–700 nm range. 10 μM carbonyl cyanide 3-chlorophenylhydrazone (CCCP) was added at the end of the experiment to completely collapse the Δψ. Data are expressed as difference of background corrected TMRM fluorescence before and after CCCP depolarization.

Muscle ATP extraction and quantification. ATP was extracted from EDL muscles from either WT or CrT^{-/-} mice using the phenol-chloroform method, as previously reported [59]. ATP measurements were performed with the ATP Determination Kit (Thermo Fisher Scientific, Catalog number: A22066), following the manufacturer's instructions. Results were background corrected and normalized for muscle weight.

Statistical analysis of data. All data were analyzed for statistical significance using GraphPad Prism software. Statistical data are presented as mean ± SEM. Depending on the experiments, a Student's *t*-test, Mann-Whitney *t*-test, and one or two-way ANOVA with Bonferroni post hoc test were applied. *p* < 0.05 was considered significant.

DATA AVAILABILITY

The data generated or analyzed during this study are accessible upon reasonable request from the corresponding author.

REFERENCES

- Wallimann T, Wyss M, Brdiczka D, Nicolay K, Eppenberger HM. Intracellular compartmentation, structure and function of creatine kinase isoenzymes in tissues with high and fluctuating energy demands: the 'phosphocreatine circuit' for cellular energy homeostasis. *Biochem J*. 1992;281:21–40.
- Ellington WR. Evolution and physiological roles of phosphagen systems. *Annu Rev Physiol*. 2001;63:289–325.
- Guimaraes-Ferreira L. Role of the phosphocreatine system on energetic homeostasis in skeletal and cardiac muscles. *Einstein*. 2014;12:126–31.
- Brosnan ME, Edison EE, da Silva R, Brosnan JT. New insights into creatine function and synthesis. *Adv Enzyme Regul*. 2007;47:252–60.
- Nash SR, Giros B, Kingsmore SF, Rochelle JM, Suter ST, Gregor P, et al. Cloning, pharmacological characterization, and genomic localization of the human creatine transporter. *Recept Channels*. 1994;2:165–74.
- Sora I, Richman J, Santoro G, Wei H, Wang Y, Vanderah T, et al. The cloning and expression of a human creatine transporter. *Biochem Biophys Res Commun*. 1994;204:419–27.
- Iyer GS, Krahe R, Goodwin LA, Doggett NA, Siciliano MJ, Funanage VL, et al. Identification of a testis-expressed creatine transporter gene at 16p11.2 and confirmation of the X-linked locus to Xq28. *Genomics*. 1996;34:143–6.
- Ghirardini E, Calugi F, Sagona G, Di Vetta F, Palma M, Battini R, et al. The role of preclinical models in creatine transporter deficiency: neurobiological mechanisms, biomarkers and therapeutic development. *Genes*. 2021;12:1123.
- van de Kamp JM, Mancini GM, Salomons GS. X-linked creatine transporter deficiency: clinical aspects and pathophysiology. *J Inher Metab Dis*. 2014;37:715–33.
- Bahl S, Cordeiro D, MacNeil L, Schulze A, Mercimek-Andrews S. Urine creatine metabolite panel as a screening test in neurodevelopmental disorders. *Orphanet J Rare Dis*. 2020;15:339.
- Beard E, Braissant O. Synthesis and transport of creatine in the CNS: importance for cerebral functions. *J Neurochem*. 2010;115:297–313.
- van de Kamp JM, Betsalel OT, Mercimek-Mahmutoglu S, Abulhoul L, Grunewald S, Anselm I, et al. Phenotype and genotype in 101 males with X-linked creatine transporter deficiency. *J Med Genet*. 2013;50:463–72.
- Puusepp H, Kall K, Salomons GS, Talvik I, Mannamaa M, Rein R, et al. The screening of SLC6A8 deficiency among Estonian families with X-linked mental retardation. *J Inher Metab Dis*. 2010;33:55–11.
- deGrauw TJ, Salomons GS, Cecil KM, Chuck G, Newmeyer A, Schapiro MB, et al. Congenital creatine transporter deficiency. *Neuropediatrics*. 2002;33:232–8.
- Hahn KA, Salomons GS, Tackels-Horne D, Wood TC, Taylor HA, Schroer RJ, et al. X-linked mental retardation with seizures and carrier manifestations is caused by a mutation in the creatine-transporter gene (SLC6A8) located in Xq28. *Am J Hum Genet*. 2002;70:1349–56.
- Kleefstra T, Rosenberg EH, Salomons GS, Stroink H, van Bokhoven H, Hamel BC, et al. Progressive intestinal, neurological and psychiatric problems in two adult

- males with cerebral creatine deficiency caused by an SLC6A8 mutation. *Clin Genet*. 2005;68:379–81.
17. deGrauw TJ, Cecil KM, Byars AW, Salomons GS, Ball WS, Jakobs C. The clinical syndrome of creatine transporter deficiency. *Mol Cell Biochem*. 2003;244:45–8.
 18. Pyne-Geithman GJ, deGrauw TJ, Cecil KM, Chuck G, Lyons MA, Ishida Y, et al. Presence of normal creatine in the muscle of a patient with a mutation in the creatine transporter: a case study. *Mol Cell Biochem*. 2004;262:35–9.
 19. Skelton MR, Schaefer TL, Graham DL, Degrauw TJ, Clark JF, Williams MT, et al. Creatine transporter (CrT; SLC6A8) knockout mice as a model of human CrT deficiency. *PLoS One*. 2011;6:e16187.
 20. Baroncelli L, Alessandri MG, Tola J, Putignano E, Migliore M, Amendola E, et al. A novel mouse model of creatine transporter deficiency. *F1000Res*. 2014;3:228.
 21. Stockebrand M, Sasaki A, Das D, Hornig S, Hermans-Borgmeyer I, Lake HA, et al. A mouse model of creatine transporter deficiency reveals impaired motor function and muscle energy metabolism. *Front Physiol*. 2018;9:773.
 22. Duran-Trio L, Fernandes-Pires G, Simicic D, Grosse J, Roux-Petronelli C, Bruce SJ, et al. A new rat model of creatine transporter deficiency reveals behavioral disorder and altered brain metabolism. *Sci Rep*. 2021;11:1636.
 23. Baroncelli L, Molinaro A, Caccianto F, Alessandri MG, Napoli D, Putignano E, et al. A mouse model for creatine transporter deficiency reveals early onset cognitive impairment and neuropathology associated with brain aging. *Hum Mol Genet*. 2016;25:4186–200.
 24. Perna MK, Kokenge AN, Miles KN, Udobi KC, Clark JF, Pyne-Geithman GJ, et al. Creatine transporter deficiency leads to increased whole-body and cellular metabolism. *Amino Acids*. 2016;48:2057–65.
 25. Wawro AM, Gajera CR, Baker SA, Nirschl JJ, Vogel H, Montine TJ. Creatine transport and pathological changes in creatine transporter deficient mice. *J Inher Metab Dis*. 2021;44:939–48.
 26. Dahlstedt AJ, Katz A, Wieringa B, Westerblad H. Is creatine kinase responsible for fatigue? Studies of isolated skeletal muscle deficient in creatine kinase. *FASEB J*. 2000;14:982–90.
 27. Steeghs K, Benders A, Oerlemans F, de Haan A, Heerschap A, Ruitenbeek W, et al. Altered Ca²⁺ responses in muscles with combined mitochondrial and cytosolic creatine kinase deficiencies. *Cell*. 1997;89:93–103.
 28. Nabuurs CI, Choe CU, Veltien A, Kan HE, van Loon LJ, Rodenburg RJ, et al. Disturbed energy metabolism and muscular dystrophy caused by pure creatine deficiency are reversible by creatine intake. *J Physiol*. 2013;591:571–92.
 29. Wyss M, Kaddurah-Daouk R. Creatine and creatinine metabolism. *Physiol Rev*. 2000;80:1107–213.
 30. Walsh B, Tonkonogi M, Soderlund K, Hultman E, Saks V, Sahlin K. The role of phosphorylcreatine and creatine in the regulation of mitochondrial respiration in human skeletal muscle. *J Physiol*. 2001;537:971–8.
 31. Dzeja PP, Hoyer K, Tian R, Zhang S, Nemutlu E, Spindler M, et al. Rearrangement of energetic and substrate utilization networks compensate for chronic myocardial creatine kinase deficiency. *J Physiol*. 2011;589:5193–211.
 32. Chamberlain KA, Chapey KS, Nanescu SE, Huang JK. Creatine enhances mitochondrial-mediated oligodendrocyte survival after demyelinating injury. *J Neurosci*. 2017;37:1479–92.
 33. Gori Z, De Tata V, Pollera M, Bergamini E. Mitochondrial myopathy in rats fed with a diet containing beta-guanidine propionic acid, an inhibitor of creatine entry in muscle cells. *Br J Exp Pathol*. 1988;69:639–50.
 34. O’Gorman E, Beutner G, Wallimann T, Brdiczka D. Differential effects of creatine depletion on the regulation of enzyme activities and on creatine-stimulated mitochondrial respiration in skeletal muscle, heart, and brain. *Biochim Biophys Acta*. 1996;1276:161–70.
 35. Pellegrino MA, Canepari M, Rossi R, D’Antona G, Reggiani C, Bottinelli R. Orthologous myosin isoforms and scaling of shortening velocity with body size in mouse, rat, rabbit and human muscles. *J Physiol*. 2003;546:677–89.
 36. Wallimann T, Tokarska-Schlattner M, Schlattner U. The creatine kinase system and pleiotropic effects of creatine. *Amino Acids*. 2011;40:1271–96.
 37. Boncompagni S, Rossi AE, Micaroni M, Beznoussenko GV, Polishchuk RS, Dirksen RT, et al. Mitochondria are linked to calcium stores in striated muscle by developmentally regulated tethering structures. *Mol Biol Cell*. 2009;20:1058–67.
 38. Perry SW, Norman JP, Barbieri J, Brown EB, Gelbard HA. Mitochondrial membrane potential probes and the proton gradient: a practical usage guide. *Biotechniques*. 2011;50:98–115.
 39. D’Angelo D, Vecellio Reane D, Raffaello A. Neither too much nor too little: mitochondrial calcium concentration as a balance between physiological and pathological conditions. *Front Mol Biosci*. 2023;10:1336416.
 40. Sartori R, Romanello V, Sandri M. Mechanisms of muscle atrophy and hypertrophy: implications in health and disease. *Nat Commun*. 2021;12:330.
 41. Farr CV, El-Kasaby A, Freissmuth M, Susic S. The creatine transporter unfolded: a knotty premise in the cerebral creatine deficiency syndrome. *Front Synaptic Neurosci*. 2020;12:588954.
 42. Udobi KC, Kokenge AN, Hautman ER, Ullio G, Coene J, Williams MT, et al. Cognitive deficits and increases in creatine precursors in a brain-specific knockout of the creatine transporter gene *Slc6a8*. *Genes Brain Behav*. 2018;17:e12461.
 43. Russell AP, Ghobrial L, Wright CR, Lamon S, Brown EL, Kon M, et al. Creatine transporter (SLC6A8) knockout mice display an increased capacity for in vitro creatine biosynthesis in skeletal muscle. *Front Physiol*. 2014;5:314.
 44. Tullson PC, Rush JW, Wieringa B, Terjung RL. Alterations in AMP deaminase activity and kinetics in skeletal muscle of creatine kinase-deficient mice. *Am J Physiol*. 1998;274:C1411–6.
 45. Ciciliot S, Rossi AC, Dyar KA, Blaauw B, Schiaffino S. Muscle type and fiber type specificity in muscle wasting. *Int J Biochem Cell Biol*. 2013;45:2191–9.
 46. Chan MC, Arany Z. The many roles of PGC-1 α in muscle-recent developments. *Metabolism*. 2014;63:441–51.
 47. Protasi F, Pietrangelo L, Boncompagni S. Improper remodeling of organelles deputed to Ca(2+) handling and aerobic ATP production underlies muscle dysfunction in ageing. *Int J Mol Sci*. 2021;22:6195.
 48. Pietrangelo L, D’Incecco A, Ainbinder A, Michelucci A, Kern H, Dirksen RT, et al. Age-dependent uncoupling of mitochondria from Ca2(+) release units in skeletal muscle. *Oncotarget*. 2015;6:35358–71.
 49. Filipe A, Chernourudskiy A, Arbogast S, Varone E, Villar-Quiles RN, Pozzer D, et al. Defective endoplasmic reticulum-mitochondria contacts and bioenergetics in SEPNI1-related myopathy. *Cell Death Differ*. 2021;28:123–38.
 50. Gherardi G, Nogara L, Ciciliot S, Fadini GP, Blaauw B, Braghetta P, et al. Loss of mitochondrial calcium uniporter rewires skeletal muscle metabolism and substrate preference. *Cell Death Differ*. 2018;26:362–81.
 51. Mammucari C, Gherardi G, Zamparo I, Raffaello A, Boncompagni S, Chemello F, et al. The mitochondrial calcium uniporter controls skeletal muscle trophism in vivo. *Cell Rep*. 2015;10:1269–79.
 52. Loud AV. A Method for the Quantitative Estimation of Cytoplasmic Structures. *J Cell Biol*. 1962;15:481–7.
 53. Mobley BA, Eisenberg BR. Sizes of components in frog skeletal muscle measured by methods of stereology. *J Gen Physiol*. 1975;66:31–45.
 54. Vannini E, Maltese F, Olimpico F, Fabbri A, Costa M, Caleo M, et al. Progression of motor deficits in glioma-bearing mice: impact of CNF1 therapy at symptomatic stages. *Oncotarget*. 2017;8:23539–50.
 55. Burkholder TJ, Fingado B, Baron S, Lieber RL. Relationship between muscle fiber types and sizes and muscle architectural properties in the mouse hindlimb. *J Morphol*. 1994;221:177–90.
 56. Hill AV. The heat of shortening and the dynamic constants of muscle. *Proc R Soc Lond B Biol Sci*. 1938;126:136–95.
 57. Rao X, Huang X, Zhou Z, Lin X. An improvement of the 2 Δ (-delta delta CT) method for quantitative real-time polymerase chain reaction data analysis. *Bio-stat Bioinform Biomath*. 2013;3:71–85.
 58. Pendin D, Norante R, De Nadai A, Gherardi G, Vajente N, Basso E, et al. A Synthetic fluorescent mitochondria-targeted sensor for ratiometric imaging of calcium in live cells. *Angew Chem Int Ed Engl*. 2019;58:9917–22.
 59. Chida J, Yamane K, Takei T, Kido H. An efficient extraction method for quantitation of adenosine triphosphate in mammalian tissues and cells. *Anal Chim Acta*. 2012;727:8–12.

ACKNOWLEDGEMENTS

We thank the staff of the mechanical workshop of the Department of Physics and Astronomy (University of Florence) for mechanical engineering support. This research was supported with funding from the Italian Ministry of University and Research (MUR), PRIN 20207P85MH to AR and ML, Next Generation EU-DM 1557, 11.10.2022, in the context of the National Recovery and Resilience Plan (NRRP), Investment PE8—Project Age-It: “Ageing Well in an Ageing Society” to ML, National Center for Gene Therapy and Drugs Based on RNA Technology, funded in the framework of the NRRP, Mission 4, Component 2, Investment 1.4, funded by the European Union - Next Generation EU, Project CN00000041, CUP C93C22002780006, Spoke n. 4 “Metabolic and Cardiovascular diseases” to RR, ECS_00000017 MUR Directorial Decree n.1055, 23 June 2022, CUP B83C22003930001, “Tuscany Health Ecosystem – THE”, Spoke 8 and Italian Ministry of Health, and RC 2023 to LB. DVR was supported by European Union funding program Horizon Europe (HORIZON-MSCA-2021-PF Project ID 101065790).

AUTHOR CONTRIBUTIONS

IP, DDA, MC, Investigation, Visualization and Writing—Original Draft; DVR, MR EP, DN, GR, IM, ADM, and GG. Investigation, SB, LB, and RR. Resources, Writing – Review & Editing and Conceptualization; ML and AR, Conceptualization, Writing – Original Draft, Writing – Review & Editing. All authors read and approved the final manuscript.

COMPETING INTERESTS

The authors declare no competing interests.

ETHICS APPROVAL AND CONSENT TO PARTICIPATE

All animal procedures were performed at the University of Padova and the University of Florence in accordance with the Italian law D. L.vo n.26/2014 and with the Directive 2010/63/EU of the European Parliament on the protection of animals used for scientific purposes. All methods were performed in accordance with the relevant guidelines and regulations.

ADDITIONAL INFORMATION

Supplementary information The online version contains supplementary material available at <https://doi.org/10.1038/s41419-025-07381-x>.

Correspondence and requests for materials should be addressed to Marco Caremani or Anna Raffaello.

Reprints and permission information is available at <http://www.nature.com/reprints>

Publisher's note Springer Nature remains neutral with regard to jurisdictional claims in published maps and institutional affiliations.



Open Access This article is licensed under a Creative Commons Attribution 4.0 International License, which permits use, sharing, adaptation, distribution and reproduction in any medium or format, as long as you give appropriate credit to the original author(s) and the source, provide a link to the Creative Commons licence, and indicate if changes were made. The images or other third party material in this article are included in the article's Creative Commons licence, unless indicated otherwise in a credit line to the material. If material is not included in the article's Creative Commons licence and your intended use is not permitted by statutory regulation or exceeds the permitted use, you will need to obtain permission directly from the copyright holder. To view a copy of this licence, visit <http://creativecommons.org/licenses/by/4.0/>.

© The Author(s) 2025